


Article

Thickening of T_1 Precipitates during Aging of a High Purity Al–4Cu–1Li–0.25Mn Alloy

Ines Häusler^{1,2}, Reza Darvishi Kamachali³, Walid Hetaba^{4,5} and Birgit Skrotzki^{1,*} 

¹ Federal Institute for Materials Research and Testing (BAM), Department 5: Materials Engineering, 12205 Berlin, Germany; haeusler@tu-berlin.de

² Institute of Optics and Atomic Physics, Technical University of Berlin, 10623 Berlin, Germany

³ Max-Planck-Institut für Eisenforschung GmbH, Max-Planck-Straße 1, 40237 Düsseldorf, Germany; kamachali@mpie.de

⁴ Department of Inorganic Chemistry, Fritz-Haber-Institute of the Max-Planck-Gesellschaft, 14195 Berlin, Germany; hetaba@fhi-berlin.mpg.de

⁵ Department of Heterogeneous Reactions, Max-Planck-Institute for Chemical Energy Conversion, 45470 Mülheim an der Ruhr, Germany

* Correspondence: Birgit.skrotzki@bam.de; Tel.: +49-308-104-1520

Received: 2 December 2018; Accepted: 16 December 2018; Published: 21 December 2018



Abstract: The age hardening response of a high-purity Al–4Cu–1Li–0.25Mn alloy (wt. %) during isothermal aging without and with an applied external load was investigated. Plate shaped nanometer size T_1 (Al_2CuLi) and θ' (Al_2Cu) hardening phases were formed. The precipitates were analyzed with respect to the development of their structure, size, number density, volume fraction and associated transformation strains by conducting transmission electron microscopy (TEM) and scanning transmission electron microscopy (STEM) studies in combination with geometrical phase analysis (GPA). Special attention was paid to the thickening of T_1 phase. Two elementary types of single-layer T_1 precipitate, one with a Li-rich (Type 1) and another with an Al-rich (Defect Type 1) central layer, were identified. The results show that the Defect Type 1 structure can act as a precursor for the Type 1 structure. The thickening of T_1 precipitates occurs by alternative stacking of these two elementary structures. The thickening mechanism was analyzed based on the magnitude of strain associated with the precipitation transformation normal to its habit plane. Long-term aging and aging under load resulted in thicker and structurally defected T_1 precipitates. Several types of defected precipitates were characterized and discussed. For θ' precipitates, a ledge mechanism of thickening was observed. Compared to the normal aging, an external load applied to the peak aged state leads to small variations in the average sizes and volume fractions of the precipitates.

Keywords: Al–Cu–Li–alloy; precipitation; T_1 precipitate; microstructure evolution; thickening; creep; volume fraction; number density; strain difference

1. Introduction

Al–Li base alloys represent an attractive material class for weight critical applications in aviation and space flight industry. These includes, e.g., fuselage and upper wing structures or cryogenic tanks [1]. These alloys are mainly strengthened by precipitation hardening. In the Al–Cu–Li system, δ' (Al_3Li), θ' (Al_2Cu) and T_1 (Al_2CuLi) are the main phases that contribute to the precipitation hardening [2–8]. The presence and amount of these phases strongly depend on the heat treatment and Cu/Li ratio in the alloy composition [2,9]. While the precipitation of δ' and θ' phases have been comprehensively investigated, the mechanism of formation and growth of the T_1 phase is still under debate. In some early studies, Nobel and Thompson [2] and Cassada et al. [10,11] proposed

that the nucleation, growth and thickening of T_1 precipitate occur by dissociation of dislocations and propagation of ledge kinks. This mechanism assumes T_1 as a four-layer platelet structure in accordance with Howe et al. [12] who proposed a structure for T_1 phase correcting an earlier structure suggested by Huang and Ardell [13]. In the light of advanced electron microscopy, however, a more complex structure for the T_1 phase has been observed that also motivates possible revision of previous theories of growth for the T_1 phase: Recent studies on the single-layer T_1 precipitate could be best explained by a model proposed by van Smaalen [14], while the earlier models by Huang and Ardell [13] and Howe et al. [12], based on which the growth mechanism for T_1 precipitate is described, are completely ruled out. This was first discussed by Donnadiou et al. [15] using scanning transmission electron microscopy (STEM) and small angle X-ray scattering (SAXS) studies, and later confirmed independently by Dwyer et al. [16] using STEM and density functional theory (DFT) studies. The characteristic feature of van Smaalen's model is the corrugated arrangement of the atomic layers parallel to the precipitate plane which suggest large rearrangement of atoms corresponding to the $\{111\}$ parent planes in the Al Matrix. Very recently, Kim et al. [17] performed DFT calculations and proposed a modified version of the van Smaalen structure, in which the arrangement of Li atoms in the interface layer are different from all previous models. Using a cluster expansion approach, they also found the possible stable T_1 phase. The calculations, however, are at 0 K and still do not fit in the phase diagram of the ternary Al–Cu–Li system.

The thickening of the T_1 precipitates seems to be an even more complex problem: It is typically observed that the T_1 phase first forms as a thin platelet precipitate (single-layer) quite stable in its thickness while it grows normally along its edge [10]. The thickness of a single-layer T_1 precipitate is found to be less than 1 nm differing for different alloy compositions [18]. At elevated temperatures or very long aging times, an abrupt thickening of T_1 precipitate has been observed, seemingly by integer multiplication of the initial T_1 single-layers accompanied by strong composition variations normal to the precipitate plate [10,11,19]. The details of this thickening were not investigated in detail in the previous studies. In particular, the structure and composition of the precipitate/matrix interface, on which the thickening occurs, is still unclear. Although it was found that, in agreement to the van Smaalen's structure, an Al–Li layer bridges the precipitate to the Al matrix phase [16], the interface layer is also evidenced to be distorted, being closer to the atomic structure of the Al matrix [15]. Hence, it is not known whether this layer belongs to the precipitate or to the Al matrix phase. In addition, segregation of secondary solute elements such as Ag has been observed [20,21], which suggests a higher energy state of the precipitate–matrix interface.

The effects of transformation strains and external stresses on the evolution of precipitates in Al alloys are widely known [22–30]. For the T_1 precipitate, it is known that dislocations may play a role in both nucleation and growth. Cassada et al. [11] showed that stretching the solutionized material prior to aging at 190 °C can largely assist with the nucleation and formation of T_1 precipitates and argued that dislocation formation and dissociation play a critical role in its thickening. Atom Probe Tomography (APT) studies revealed that segregation of Mg and Cu at the dislocations correlates with nucleation of T_1 precipitates [21]. However, formation of the T_1 phase without predeformation has also been reported [5]. Other structural defects can also play a role in the T_1 precipitation process [31]. A defected T_1 structure can form due to the interaction with dislocations. It is found that T_1 precipitates can be sheared by dislocations even when they reach a thickness of several nanometers [32], which improves the formability of the alloy. The stable and small thickness of the T_1 precipitates indicates a large elastic anisotropy of this phase, but the strain associated to its formation is not yet fully uncovered due to the unknown phase structure.

In this study, comprehensive transmission electron microscopy (TEM), high resolution scanning transmission electron microscopy (HR-STEM) and geometrical phase analysis (GPA) measurements were conducted to gain insights regarding the evolution of T_1 and θ' precipitates. Special attention was paid to the formation and thickening of the T_1 phase. We considered a rather high-purity model alloy (Al–4Cu–1Li–0.25Mn alloy (wt. %)) that is similar to the technical alloy AA2195 with respect

to Cu, Li and Mn, but does not contain secondary alloying elements. The high purity allowed better characterization of the precipitation mechanisms without the accelerating effects due to additional alloying elements [20,21]. In this alloy, both T_1 and θ' may form and grow. The details of peak hardening response of the current alloy have been previously studied [33]. In the current study, we extended the previous work by investigating long term aging and aging under external load (creep conditions). In particular, the layering sequence of T_1 phase and the role of the interfacial layer during its thickening were discussed. The strains normal to the T_1 precipitate plane were measured along the thickening of the precipitate. The effect of external load on the evolution of these precipitates were studied as well. A mechanism of thickening was proposed for the T_1 phase that is associated with the transformation strain accompanying the process. Different defected structures of T_1 phase were identified and analyzed as well. Furthermore, the size evolution of both T_1 and θ' precipitates was studied in detail.

2. Materials and Methods

2.1. Material and Sample Preparation

The investigated aluminum alloy has a nominal chemical composition of 4% Cu, 1% Li and 0.25% Mn (wt. %; balance Al). The amount of impurities is less than 0.06% [33] (i.e., 0.012 Si, <0.006 Fe, 0.007 Mg, <0.001 Ni, <0.009 Zn, 0.003 Co, 0.004 Sn, 0.005 Bi, 0.0031 Cd, and all other elements < 0.001; all in wt. %). High-purity elements were molten in a vacuum induction furnace and poured into a water-cooled crucible under argon atmosphere. The cast was homogenized at 515 °C for 24 h, water quenched and subsequently extruded at 420 °C (profile cross-section: 15 mm × 70 mm). The final heat treatment process was solutionizing of the profile at 505 °C for 70 min, followed by water quenching. At last, the extruded profiles were stretched by about 2.9% to straighten them. The resulting material was received as semi-finished block profiles with dimensions of 15 mm × 70 mm × 655–785 mm. This material state is designated as “initial state” in the following.

The strand was cut into 100 mm long sections, which were afterwards thermally aged to the peak aged (PA) state. The aging was carried out at 180 °C for 17 h in a radiation furnace (ATS model 3710, Applied Test System, Inc. (ATS; Butler, PA, USA); maximum temperature deviation: ± 5 °C) according to parameters defined in [33]. Subsequently, coupons and creep specimens were machined from the section, as shown in Figure 1a,b. The dimensions of the coupons, which were used for hardness measurements and serve as isothermally and load-free aged reference samples during the study (called reference sample in the following), were 22 mm × 15 mm × 5 mm. The longitudinal axis of the creep specimens corresponds to the L-axis of the profile. The geometry of the creep specimens is given in Figure 1c. The gauge diameter was 8 mm, while the gauge length was 50 mm.

Table 1 summarizes the conditions (and sample designations) investigated in this paper. *Ref. 0* represents the peak aged (PA) state. The remaining samples received a further isothermal aging treatment after the PA treatment: samples *Ref. 1* and *Ref. 2* were aged at 180 °C for 257 h and 1002 h, respectively. Samples *Creep test 1* and *Creep test 2* were aged under an external load of 155 MPa at the same temperature and for the same time as *Ref. 1* and *Ref. 2*. Aging under load was realized in a standard creep testing rig (constant load lever arm machine, 20 kN capacity). The length change Δl of the specimens was recorded using an extensometer system and then converted into strain ($\varepsilon = \Delta l/l_0$).

The hardness was measured for both the coupons and the creep specimens on the ST-LT plane. The surface was ground with SiC abrasive paper (grit size P600, P1200, P2400) and subsequently polished with diamond suspension (particle size 3 μm and 1 μm). Brinell hardness was determined following DIN EN ISO 6506-1 [34] using hardness tester M4C 025 G3 (EMCO-TEST, Kuchl, Austria). The testing parameters were: ball diameter 2.5 mm, test force 612.9 N, and exposure time between 10 s and 15 s.

For the transmission electron microscopy (TEM) investigation of the creep specimens, samples were cut from the center of the gauge section parallel to the external loading direction (i.e., in the

L-LT-plane). Samples of the reference states were taken from the coupons in L-LT-plane. After sawing, all TEM specimens were prepared by conventional technique (grinding and polishing of both sides down to 100 μm , and punching of discs with 3 mm diameter). Finally, the discs were electro-polished using a solution of methanol (CH_3OH) and nitric acid (HNO_3) at a ratio of 2:1 at $-23\text{ }^\circ\text{C}$.

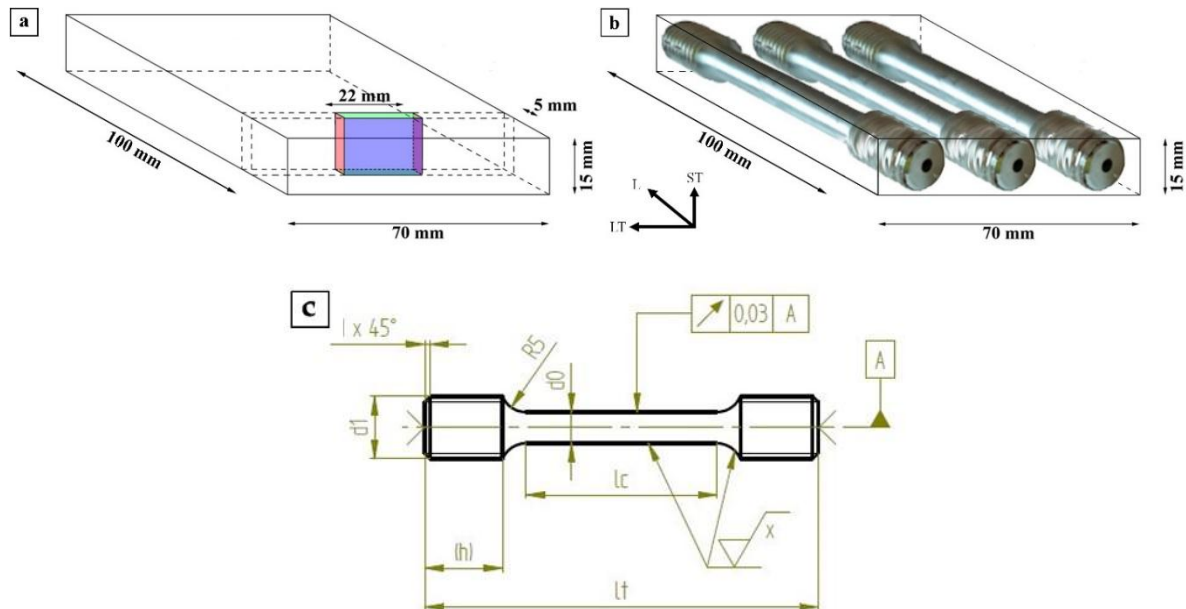


Figure 1. Sampling of specimens from the extruded profile (L, longitudinal direction; LT, long transverse direction; ST, short transverse direction): (a) coupons for aging treatments; (b) creep specimens; and (c) creep specimen geometry with dimensions of $d_0 = 8\text{ mm}$, $d_1 = \text{M12}$, $l_c = 60\text{ mm}$, $l_t = 100\text{ mm}$, and $(h) = 15\text{ mm}$. Surface finish: $R_z = 3.2$.

Table 1. Sample designation and investigated material states.

| Sample | Pre-Treatment | External Load (MPa) | Temperature ($^\circ\text{C}$) | Time (h) |
|--------------|---------------------------------|---------------------|----------------------------------|----------|
| Ref. 0 | PA (17 h/180 $^\circ\text{C}$) | - | - | - |
| Ref. 1 | PA (17 h/180 $^\circ\text{C}$) | - | 180 | 257 |
| Ref. 2 | PA (17 h/180 $^\circ\text{C}$) | - | 180 | 1002 |
| Creep test 1 | PA (17 h/180 $^\circ\text{C}$) | 155 | 180 | 257 |
| Creep test 2 | PA (17 h/180 $^\circ\text{C}$) | 155 | 180 | 1002 |

High-angle annular dark-field (HAADF) scanning TEM (STEM) images were recorded using the STEM/TEM microscope 2200FS (JEOL, Tokyo, Japan) (acceleration voltage: 200 keV; equipped with an in-column-energy filter and a HAADF detector) at the Federal Institute for Materials Research and Testing (BAM). After recording the HAADF-STEM images, a thickness map of the same area was taken. For this purpose, the area was divided into a grid of 20×20 points. The recording and analysis of the low loss region of the electron energy loss spectrum (EELS) of each point of the grid enables the determination of the TEM foil thickness within the grid in terms of units of “mean-free path length” of aluminum [35]. Both convergent beam electron diffraction (CBED) patterns and EEL spectra at the same position were recorded and analyzed for conversion from “mean-free path length” into “nm” [35,36]. The evaluation revealed a mean-free path length of 137 nm [33]. The high-resolution HAADF-STEM images were recorded at the Fritz Haber Institute of the Max Planck Society, Berlin, using the double-corrected JEOL microscope JEM ARM200F (200 keV; equipped with image Cs-corrector, probe Cs-corrector, Gatan imaging filter (GIF) and HAADF detector).

2.2. Quantification of Precipitate Dimensions and Determination of Strain Field within and Around Precipitates Using GPA

To quantify the development of the precipitate size during the aging process, $[110]_{\text{Al}}$ oriented STEM dark field images of areas with a foil thickness, t , of approximately 150–200 nm were recorded for different aging treatments. In this orientation, two variants of T_1 and one variant of θ' are edge on (i.e., parallel to the electron beam) [33]. Therefore, the length (diameter) and width (thickness) of the plate shaped precipitates can be measured and used as an indicator of the growth process.

When quantitatively comparing precipitates of different aging conditions, it is necessary to take into account that the disk-shaped precipitates in the investigated volume are for the most part truncated due to the thinness of the TEM foil. Therefore, line lengths of precipitates in $[110]_{\text{Al}}$ oriented images correspond to the true precipitate diameter only if the center of the precipitate is within the TEM foil. Otherwise, the line length represents the length of a chord. To allow a direct comparison between the different samples and aging conditions, it is necessary that the TEM foil thickness is approximately the same. For quantification of line lengths and number density as a function of time, $[110]_{\text{Al}}$ oriented HAADF-STEM overview images of regions with a thickness between 150 nm and 200 nm were analyzed. Due to the chosen $[110]_{\text{Al}}$ orientation, only those precipitates that are lying on the $(001)_{\text{Al}}$, $(\bar{1}11)_{\text{Al}}$ and $(1\bar{1}1)_{\text{Al}}$ planes were imaged. Thus, precipitates that are not parallel to the incoming electron beam are not considered in the quantitative analysis. Therefore, only one third of the θ' -precipitates and only half of the T_1 -precipitates are imaged in $[110]_{\text{Al}}$ orientation [33]. This needs to be corrected on calculating the number densities and volume fractions of the precipitates by multiplying by a factor of 3 (for θ') and 2 (for T_1), respectively.

It was not possible to determine the length of the precipitates based on their gray scale contrast to the matrix using an automatic software-based method, since gray scales varied locally within each image. Therefore, the precipitates were traced manually on three separate image planes (using the software Photoshop), i.e., each family of precipitate orientation on one plane (see Figure 13 in [37]). This results in three images with discrete gray scale values which can be analyzed by image analysis software Esprit (version 1.9, Bruker Nano GmbH, Berlin, Germany). Besides line length, the x and y coordinates of the center of gravity of the line were also determined for each precipitate.

The thickness of each x, y position was determined by EELS (see Section 2.1). The thickness of individual precipitates was determined from high-resolution HAADF-STEM images (see Section 2.1) and a mean value was calculated for the volume fraction calculation. For each condition, about 300 to 400 T_1 and about 250 θ' precipitates were considered.

A procedure was developed by Häusler [37] to determine the volume fraction of oriented disk shaped precipitates from 2D projections of a 3D volume as recorded in the TEM. Detailed derivation and validation are given there and are not repeated here. The volume fraction of the counted precipitates was calculated using the following equation [37]:

$$\begin{aligned}
 & f_V(s_i, c_i, t) \\
 &= 100\% \sum_{i=1}^N \frac{1}{2} \left[\left\{ \frac{\left(\frac{t}{0.5665 \cdot s_i + t} \right) \left(\pi \left(\frac{s_i}{2} \right)^2 c_i \right) + \left(\frac{0.5665 \cdot s_i}{0.5665 \cdot s_i + t} \right) (0.8276 \cdot s_i^2 c_i)}{\text{area} \cdot (0.5665 \cdot s_i + t)} \right\} \right. \\
 & \left. + \left\{ \frac{\left(\frac{t}{1.133 \cdot s_i + t} \right) \left(\pi \left(\frac{s_i}{2} \right)^2 c_i \right) + \left(\frac{1.133 \cdot s_i}{1.133 \cdot s_i + t} \right) (0.8276 \cdot s_i^2 c_i)}{\text{area} \cdot (1.133 \cdot s_i + t)} \right\} \right] \quad (1)
 \end{aligned}$$

with: s_i length of the line i

c_i thickness of the line i

t_i TEM foil thickness in the center of the line i

area size of the investigated area (i.e., the area of the TEM image)

Since the determination of c_i for each precipitate is not possible, an average \bar{c} was calculated. Up to 10 precipitates of each precipitate type and each aging treatment were recorded using HR-STEM images and the corresponding arithmetic mean value \bar{c} was calculated.

Finally, the volume fraction, f_v , combined with the thickness and the diameter of the precipitates allowed calculating the number density, N , of the precipitates per unit volume using the following equation [19]:

$$N = \frac{4 \cdot f_v}{\pi \cdot \bar{c} \cdot \bar{s}^2} \quad (2)$$

with \bar{c} being the mean thickness of precipitates and \bar{s} the mean line length of precipitates.

To obtain the strain fields within and around T_1 precipitates, high-resolution HAADF-STEM images in $[110]_{Al}$ orientation were evaluated by means of geometric phase analysis (GPA) [38] using the software ImageEval (University Bremen, Germany [39]). The GPA procedure is described in Figure 2. Before starting the strain analysis, the HAADF-STEM image was rotated to orient the precipitate in a horizontal position (Figure 2a). Then, an image area far from the precipitate with a defect free and unstrained structure was selected. This region was the reference area required for the analysis, and is abbreviated in the following with REF (see REF area in green in Figure 2a). Thereafter, the image was Fourier transformed, and subsequently the two linearly independent aluminum reflections $g_1 = \bar{1}11$ and $g_2 = 00\bar{2}$ were selected by a mask in the FFT image (Figure 2b; mask parameters: cosine damping and width of damping function in “units of mask radius” is 0.1). The two-dimensional phase images 1 and 2 were calculated (Figure 2c,d) based on the pixels within the mask area around the corresponding reflections 1 and 2. Finally, the two dimensional strain maps ε_{xx} , ε_{yy} and ε_{xy} (see Figure 2e–g) were calculated from phase images 1 and 2.

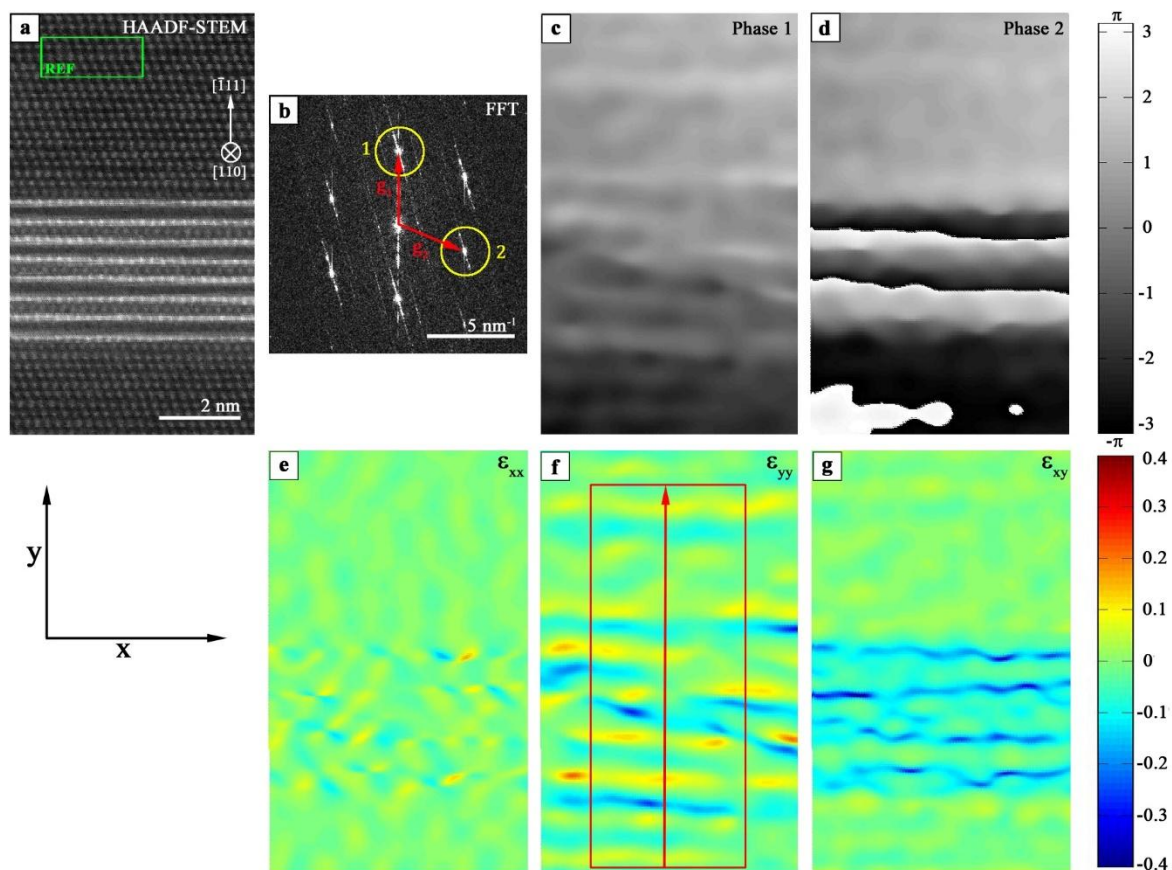


Figure 2. GPA procedure applied to a T_1 precipitate (Type 4): (a) high-resolution HAADF-STEM image with reference area (REF) marked in green; (b) Fourier transformed HAADF-image with marked reflections 1 and 2 ($g_1 = \bar{1}11$ and $g_2 = 00\bar{2}$); (c,d) calculated two-dimensional phase images 1 and 2 using reflections 1 and 2 in (b); and (e–g) two-dimensional strain maps ε_{xx} , ε_{yy} and ε_{xy} . Scale bar in (c) and (d) is the same as in (a).

The strain fields within and around the precipitate correspond to the structural mismatch between fcc Al matrix and complex T_1 precipitate. For better comparison of individual strain fields perpendicular to the precipitate–matrix interface, a line profile including error bars was generated across the two-dimensional ε_{yy} strain field within the rectangular region marked in red. For the line profile, the strain values inside the rectangle were averaged along the x-direction and the corresponding standard deviations were calculated. The extreme values $\varepsilon_{yy,min}$ and $\varepsilon_{yy,max}$ were extracted from the one-dimensional ε_{yy} strain profile (see Figure 3) and used to calculate the amplitude, i.e., $\varepsilon_{yy,max}-\varepsilon_{yy,min}$. This amplitude value reflects the distortion and, therefore the strain between the lattice planes in y-direction with respect to the reference area (fcc Al matrix). These values are used for the direct comparison of the strain in and around T_1 precipitates of different types and thickness.

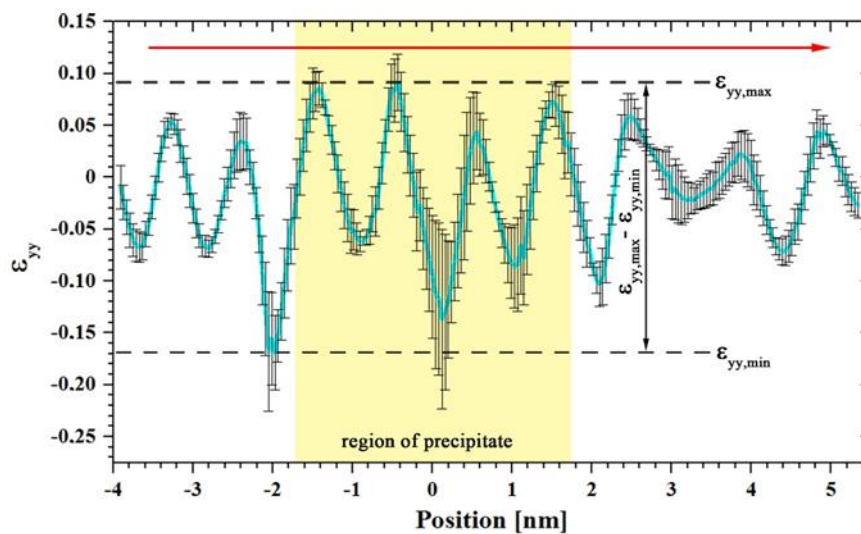


Figure 3. Line profile across the ε_{yy} strain map shown in Figure 2f.

3. Results

The microstructure of the initial state is characterized by elongated grains in L-direction (Figure 1) due to the extrusion process (not shown). The quantitative analysis of the grain sizes using the linear intercept method resulted in an average length of about 1111 μm and an average width of about 505 μm for the LT-ST plane (cf. Figure 1).

3.1. Creep Behavior

These tests primarily served to realize aging under an external load. Figure 4 shows the creep curves of the PA state obtained at a nominal stress of 155 MPa at 180 °C (*Creep test 1* and 2). The two curves in Figure 4a almost coincide, which indicates the good reproducibility of the tests. *Creep test 1* was terminated after reaching 0.10% strain, and *Creep test 2* at 0.28% strain. From the creep strain evolution in Figure 4a, the creep rate, $\dot{\varepsilon}$, was calculated and plotted vs. creep strain, ε (Figure 4b). The figures show that both creep specimens were deformed to the secondary creep stage in which the creep rate is nearly constant.

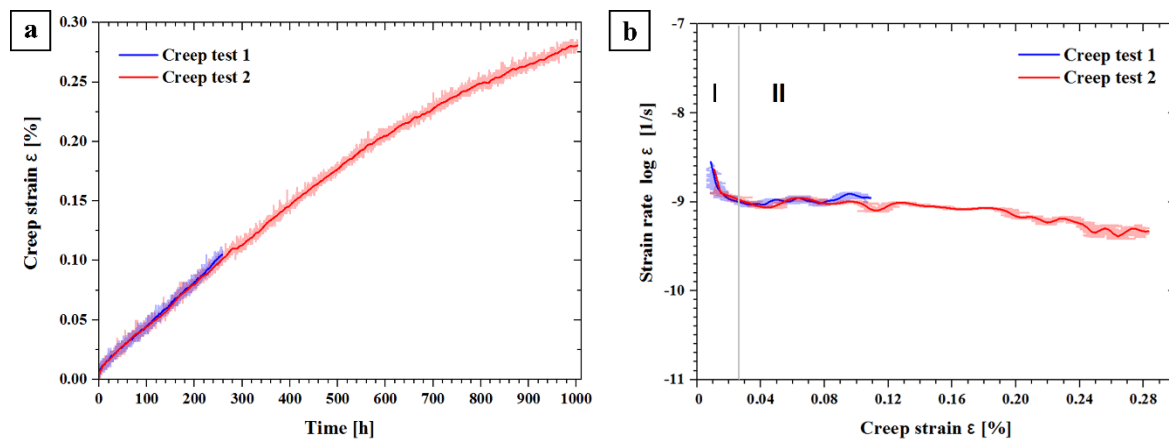


Figure 4. (a) Creep strain vs. time; and (b) strain rate vs. creep strain with creep stage I (primary) and II (secondary).

3.2. Brinell Hardness

Brinell hardness measurements were carried out on the load-free aged samples and on the creep specimens to capture possible microstructural changes. Table 2 summarizes the results. During load free aging, the hardness decreases from 158 HBW in the PA state (*Ref. 0*) to 133 HBW after 257 h (*Ref. 1*) and 115 HBW after 1002 h (*Ref. 2*). Aging under applied stress (*Creep test 1* and *2*) results in similar hardness values as in the reference states.

Table 2. Brinell hardness after aging without and with stress.

| Sample | Aging/Creep Time (h) | Brinell Hardness HBW 2.5/62.5 | |
|----------------------------|----------------------|-------------------------------|-------------|
| | | load free aging | creep |
| <i>Ref. 0</i> | PA | 158 \pm 7 | - |
| <i>Ref. 1/Creep test 1</i> | PA + 257 | 133 \pm 2 | 132 \pm 2 |
| <i>Ref. 2/Creep test 2</i> | PA + 1002 | 115 \pm 3 | 116 \pm 2 |

3.3. Microstructure

3.3.1. Peak Aged State

To interpret the hardness change during the aging and creep experiments, STEM investigations of the aged samples (without and with load) were carried out and compared to the PA state.

As previously reported [33], imaging the precipitate structure in TEM in $[100]_{Al}$ and $[110]_{Al}$ zone axis clearly show that only θ' (Al_2Cu) precipitates and T_1 (Al_2CuLi) precipitates are present in the PA state and no δ' has formed. Experimental and simulated electron diffraction patterns of the PA-state are given in Figure 5. Slightly brighter dots at positions where reflections of the δ' phase should appear are θ' reflection rods lying perpendicular to the image plane. For a detailed interpretation of the diffraction patterns, see [33]. It is clear in Figure 5c,d that two variants of T_1 and one variant of θ' are edge on in the $[110]_{Al}$ orientation.

The micrograph of the PA state in Figure 6(a.1) shows a high number of plate shaped precipitates. Two variants of T_1 (Al_2CuLi) on the $\{111\}_{Al}$ planes (marked in blue in the schematic in the upper right corner) and one variant of θ' (Al_2Cu) on the $\{100\}_{Al}$ planes (marked in red) are visible. Based on high-resolution HAADF-STEM images (see Figure 7a,b), it is clear that, in this aging condition, all T_1 plates consist of two bright layers separated by a relatively darker intermediate layer.

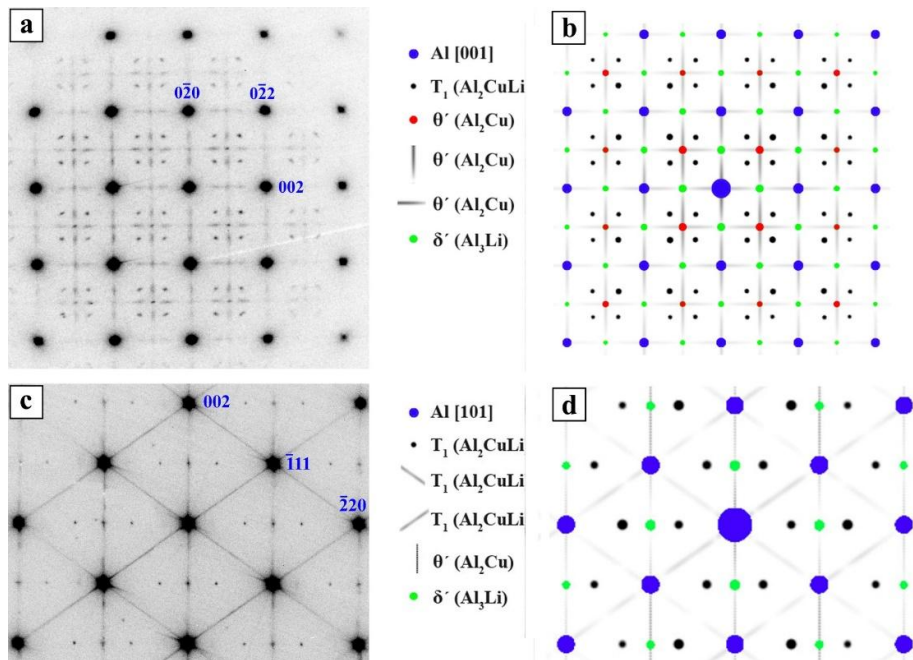


Figure 5. Energy-filtered experimental (a,c) and simulated (b,d) electron diffraction pattern of the PA state. Zone axis is $[100]_{Al}$ in (a,b), and $[110]_{Al}$ in (c,d) (adopted from [33]).

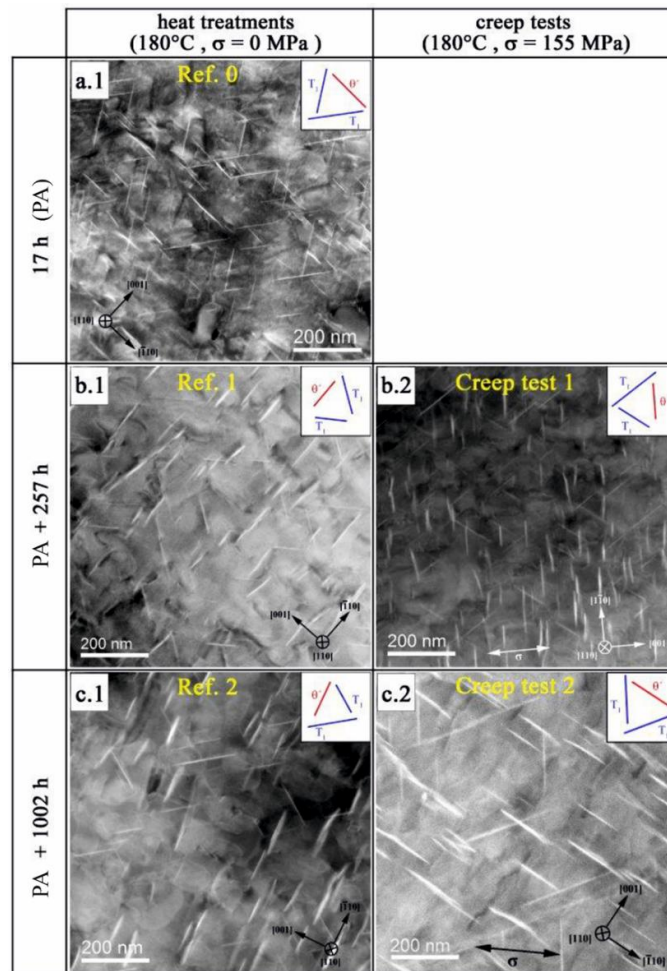


Figure 6. DF-STEM images of the microstructure as a function of aging treatment: (a.1) PA-state; (b.1,c.1) after aging without load; and (b.2,c.2) after loading under applied load (creep).

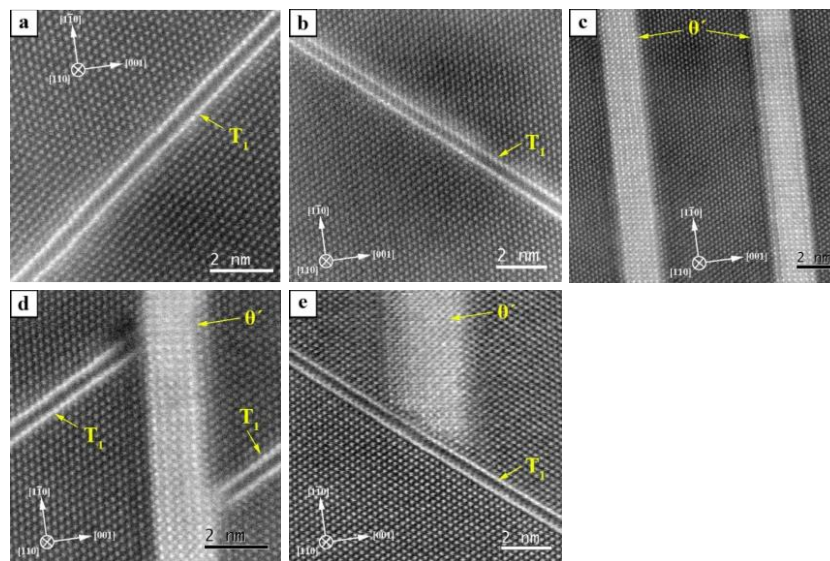


Figure 7. HR-STEM images of T_1 and θ' precipitates in the PA state: (a) T_1 precipitate on $(\bar{1}\bar{1}1)_{Al}$; (b) T_1 precipitate on $(1\bar{1}1)_{Al}$; (c) θ' precipitates on $(001)_{Al}$; (d) θ' precipitate stops the growth of two T_1 precipitates; and (e) T_1 precipitates terminates growth of a θ' precipitate.

The crystal structure of the single-layer T_1 precipitates has been the subject of several studies [12–16,40]. There are, however, still slightly different ideas on the T_1 structure. The similarity of all these structural models is the presence of a Li-rich layer surrounded by two Cu-rich layers. HAADF images of such an arrangement of atomic layers show two bright lines and a dark line in between [15,16] that were also observed in the present study. This stacking of T_1 structure dominates in the PA state and in the following such stacking (two bright layers and one dark intermediate layer) is named “Type 1” or T-1 (see Figure 8a).

In addition to the T-1, several other stacking sequences of T_1 precipitates were also found in the present study (see Figure 8). In the PA state, another T_1 stacking was found having a bright intermediate layer with an intensity similar to that of the Al matrix. It seems that the Li atoms are missing or reduced in the intermediate layer of these precipitates and it can be assumed that the intermediate layer consists of Al atoms. This structure is called “Defect Type 1” or DT-1 (see Figure 8b). The T-1 and DT-1 T_1 precipitates are 0.505 nm and 0.461 nm thick, respectively. This is in line with the fact that Li atoms are larger than Al atoms and hence their absence in the DT-1 precipitates results in a smaller thickness of the precipitate. In the PA state, 75% of T_1 precipitates are of T-1 and 25% of DT-1 (cf. Table 3). Mean thicknesses are calculated and summarized in Table 4. Interestingly, T_1 precipitates with mixed structure were observed as well.

Figure 7b shows a T_1 precipitate with mixed structure: the intermediate layer is rich in Al in the upper left region (bright intermediate layer) and rich in lithium in the lower right region (dark intermediate layer) of the image. These mixed typed precipitates were counted as both T-1 and DT-1. The two T-1 and DT-1 structures seem to be the elementary units for the T_1 phase that are frequently observed during thickening, although it seems that the DT-1 stacking is not fully stable.

Comparing the dimensions of T_1 and θ' in the PA state (Figures 6a and 7a, and Table 4), it is evident that the thickness of the θ' precipitates is much larger than that of the T_1 plates: it varies between 10 layers (1.56 nm) and 28 layers (4.4 nm) (Figure 7c). If a precipitate plate reaches another precipitate during growth, they do not penetrate each other; their length growth is rather stopped. Thus, the θ' precipitate in Figure 7d terminates the growth of two T_1 precipitates to its left and right side.

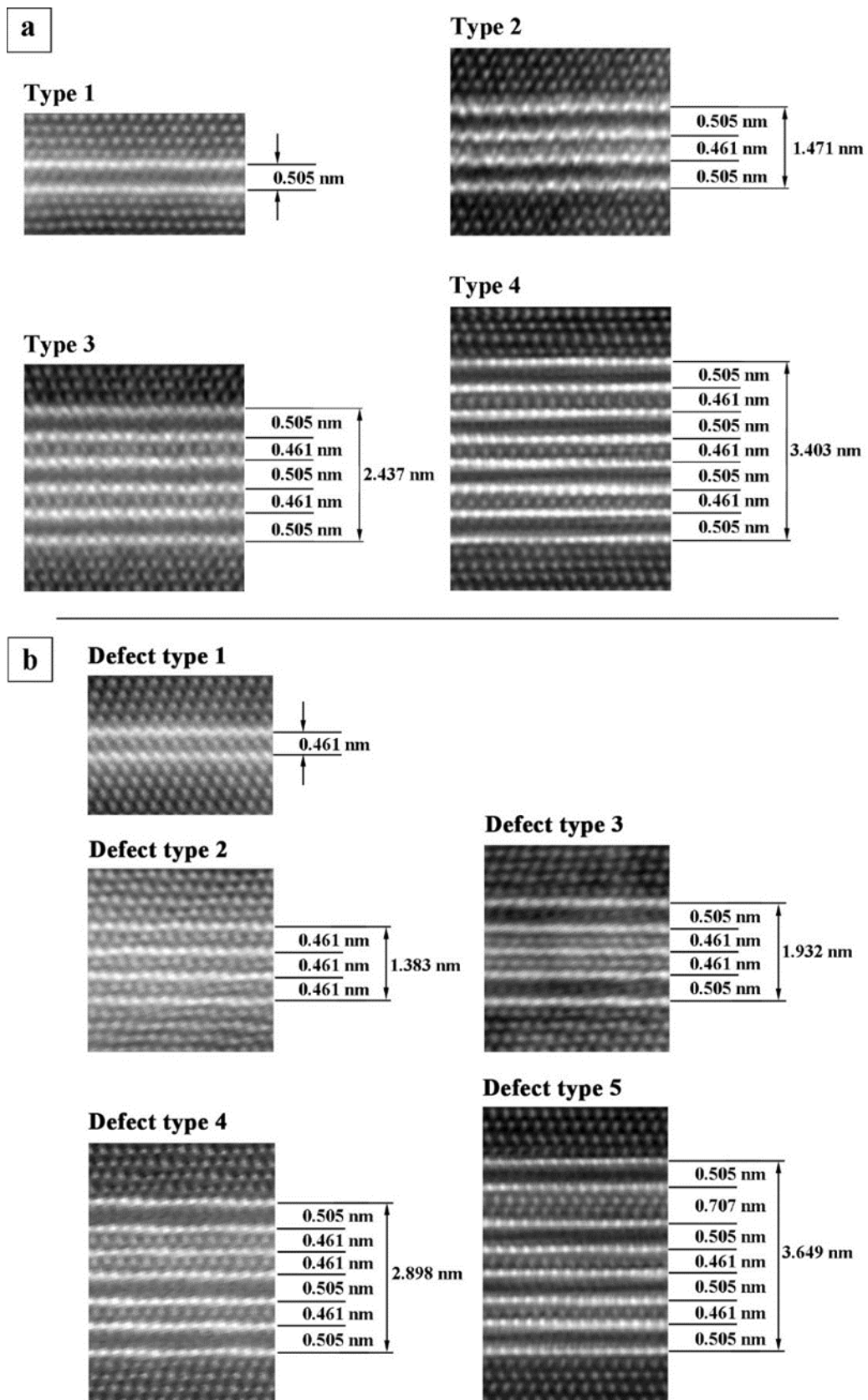


Figure 8. Types of T_1 precipitates found in both the creep specimens and in the reference samples: (a) stacking sequences without defects; and (b) stacking sequences with defects.

Table 3. Relative frequency of T_1 precipitate types after different aging treatments (see Figure 8 for details of the T_1 types and defect types).

| Specimen | T_1 Type | | | | Defect Type | | | | | Total Defects |
|---------------------|------------|-------|-----|-------|-------------|------|------|------|------|---------------|
| | T-1 | T-2 | T-3 | T-4 | DT-1 | DT-2 | DT-3 | DT-4 | DT-5 | |
| <i>Ref. 0</i> | 75% | - | - | - | 25% | - | - | - | - | 25% |
| <i>Ref. 1</i> | - | 100% | - | - | - | - | - | - | - | - |
| <i>Ref. 2</i> | - | 20% | 47% | 20% | - | - | - | 6.5% | 6.5% | 13% |
| <i>Creep test 1</i> | 21% | 52.7% | 21% | - | - | - | 5.3% | - | - | 5.3% |
| <i>Creep test 2</i> | - | 45.4% | - | 27.3% | - | 9.1% | 9.1% | - | 9.1% | 27.3% |

Table 4. Mean line length, \bar{s} , with standard deviation and mean thickness, \bar{c} , of T_1 and θ' precipitates depending on the aging treatment.

| Specimen | \bar{s} (nm) | | \bar{c} (nm) | |
|---------------------|----------------|-----------|----------------|-----------|
| | T_1 | θ' | T_1 | θ' |
| <i>Ref. 0</i> | 93 ± 41 | 68 ± 30 | 0.494 | 2.402 |
| <i>Ref. 1</i> | 76 ± 34 | 60 ± 25 | 1.471 | 4.062 |
| <i>Ref. 2</i> | 74 ± 26 | 80 ± 30 | 2.546 | 5.686 |
| <i>Creep test 1</i> | 72 ± 32 | 59 ± 27 | 1.495 | 3.648 |
| <i>Creep test 2</i> | 129 ± 64 | 91 ± 44 | 2.231 | 4.694 |

Figure 7e shows another case where a θ' precipitate meets a T_1 precipitate and is stopped as well. A recent in-situ study by Liu et al. [41] showed the interaction of precipitates in close proximity: some precipitates completely vanished, while the growth of others was accelerated after coming in contact with each other.

3.3.2. Effect of Further Aging

Further aging of the PA state at 180 °C for 257 h and 1002 h results in microstructural changes regarding mean size (\bar{c} and \bar{s}), volume fraction, f_v , number density, N , and structure of the precipitates. Figure 6a.1–c.1 shows DF-STEM images of the microstructure of the PA state and the load free aged samples (*Ref. 1* and *Ref. 2*). It is apparent that the T_1 and θ' precipitates grew during 257 h aging. In this stage, it was found that all T_1 precipitates thicken from a single layer to three layer with the same structure. The three-layer structure in this stage consists of a DT-1 layer sandwiched between two T-1 stackings. This kind of T_1 precipitate is called “Type 2” (T-2). The T-2 precipitates have a thickness of 1.471 nm = 2 × 0.505 nm + 0.461 nm (see Table 4 and Figure 8a). The fact that all observed T_1 precipitates after 257 h aging exhibit the same thickness and stacking (T-2) suggests that this structure was more stable than T-1 and DT-1 single layer precipitates. In fact, structurally, it is possible for either T-1 or DT-1 T_1 precipitates to grow and form T-2 precipitate.

The line length of the T_1 plates is approximately 76 nm, which is somewhat smaller than in the PA state (93 nm) but within the scatter of the length measurement (Table 4 and Figure 9a). Figure 9b shows that the θ' phase (red symbols) behaves similarly, the thickness increases by a factor of 1.7 and the mean line length decreases somewhat but within the experimental scatter. The number density of θ' precipitates increases by a factor of 2 as compared to the PA state, while that of the T_1 precipitates (blue symbols) decreases slightly. Thus, it is not clear whether DT-1 precipitates disappear first and nucleate on the T-1 precipitates, or whether they can thicken on their own. It is to note that this picture of the thickening slightly deviates from the previous discussions on the structure of single-layer T_1 precipitate, which assumes the interface Al layer would be part of the precipitate.

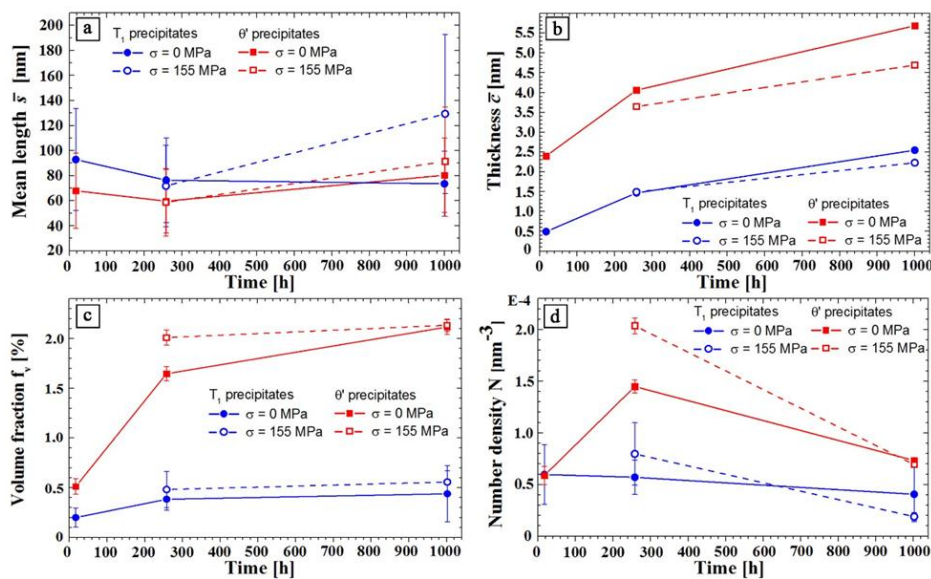


Figure 9. Evolution of the characteristics of T_1 (blue) and θ' (red) precipitates vs. aging/creep time: (a) mean line length \bar{s} ; (b) mean thickness \bar{c} ; (c) volume fraction f_v ; and (d) number density N .

Longer aging time of 1002 h leads to further thickening of θ' precipitates up to 5.686 nm and a mean line length of about 80 nm. The mean thickness of the T_1 precipitates increases to 2.546 nm but its length remains unchanged. In this case, several other types of T_1 precipitate were observed as well.

High-resolution STEM images of Ref. 2 show that the stacking height and sequence of the T_1 platelets increases markedly. Aging from 257 h to 1002 h, only 20% of T-2 stacking remain in the microstructure and the majority of the precipitates thicken in different stacking sequences (see Table 3 and Figure 8a): “Type 3” (T-3) and “Type 4” (T-4) stackings form, which consist of three and four T-1 stackings, respectively, separated by an Al-rich intermediate layer resembling the DT-1 structure. These are rather “regular” thickening of the T_1 precipitate that are also observed in previous studies (for instance [10,19]). Furthermore, some T_1 precipitates with irregular stacking frequency were found (see Table 3 and Figure 8b): Defect Type 4 (DT-4), which consists of a Type 4 stacking in which a Li-rich intermediate layer is absent; and Defect Type 5 (DT-5) that is a modified Type 4, in which one Al-rich layer is replaced by two Al-rich layers. Table 3 summarizes the frequency of the different stacking types for all investigated conditions. Closer inspection of the thickened structures suggests that all stacking sequences, except DT-5, which maintains a special structural defect, can be identified as multiple T-1 or DT-1 stackings with corresponding 0.505 nm and 0.461 nm thickness, respectively.

After 1002 h, the number density of θ' precipitates declines back to the value of the PA state, while that of T_1 is unchanged. The volume fraction of the T_1 precipitates increases only slightly (0.20% in the PA state, 0.38% after 257 h, and 0.44% after 1002 h) with time, while that of θ' shows a drastic increase from 0.51% in the PA state to 1.65% after 257 h and 2.12% after 1002 h.

3.3.3. Effect of Applied Load

The development of the microstructure under creep load is represented in Figure 6b.2,c.2 and the quantitative data are given in Figure 9.

Aging with applied stress results in only small length and thickness changes for both precipitates for 257 h compared to the load-free aging state Ref. 1. However, longer creep time (1002 h) results in growth in length direction for T_1 while the thickness remains almost unchanged. The opposite is observed for θ' : the length changes only little, while the thickness is somewhat smaller than for stress free aging. The experimental data imply that the volume fraction and the number density of T_1 phase seem not to be affected by an external stress. In contrast, creep loading for 257 h result in a 25% higher volume fraction and a 40% higher number density of θ' . It seems that the volume fractions for both

precipitates and both loading conditions (load free/creep) reach a saturated value after 1002 h, which indicates that growth processes are completed, and coarsening will start on further aging.

The structure and stacking of the T_1 precipitates, however, dramatically changes in the presence of external load. In contrast to the sample *Ref. 1* that contains only T_1 plates of T-2, the loaded counterpart of this specimen (*Creep test 1*) contains T_1 precipitates of T-1, T-3 and Defect Type 3 (DT-3) as well. In the DT-3 stacking, two DT-1 are sandwiched with two T-1 stacking sequences outside. This kind of defected structure was not observed during the load free aging even after 1002 h.

After 1002 h aging under load, Type 4 (T-4) precipitates also appeared and stacking T-3 disappeared. The T-3 and T-4 stacking can be considered as the next thickening sequence of a T_1 precipitate with T-2 structure where further thickening of T_1 precipitate occurs by sequential stacking of T-1 and DT-1. Figure 10 shows T_1 precipitates after 1002 h of creep loading. The T_1 precipitates in Figure 10a,b lie on the $(\bar{1}11)_{Al}$ planes and have a stacking of T-2 and T-4, respectively. The T_1 precipitate in Figure 10c lies on the $(1\bar{1}1)_{Al}$ and is also of T-2.

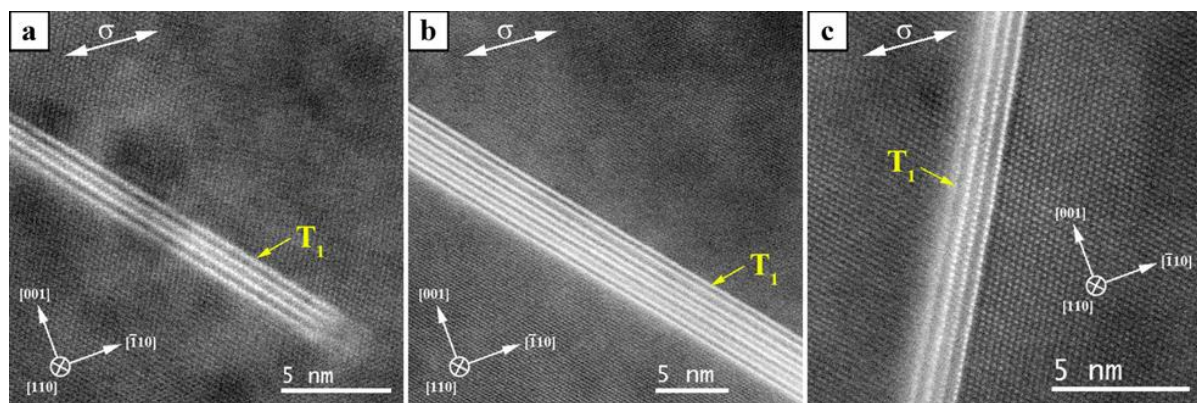
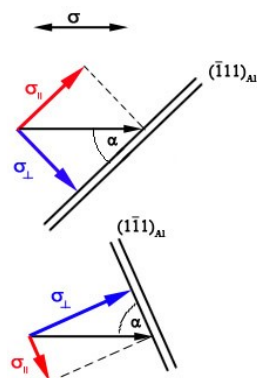


Figure 10. T_1 plates of *Creep test 2* (155 MPa, 180 °C, 1002 h): (a) Type 2 on $(\bar{1}11)_{Al}$; (b) Type 4 on $(\bar{1}11)_{Al}$; and (c) Type 2 on $(1\bar{1}1)_{Al}$.

The angle between the external load direction σ and $(\bar{1}11)_{Al}$ is about 46° , and that between σ and $(1\bar{1}1)_{Al}$ is about 64° . Despite this relatively large angle difference of about 18° , which corresponds to a load difference of approximately 28 MPa perpendicular to the T_1 precipitates interface, no differences regarding their size and thickness can be found between T_1 plates on the $(\bar{1}11)_{Al}$ and on $(1\bar{1}1)_{Al}$. The load difference was calculated by resolution of the external load σ :



$$\sigma_{\perp} = \sigma \cdot \sin\alpha$$

For the $(\bar{1}11)_{Al}$ ($\alpha = 46^\circ$ and $\sigma = 155$ MPa):
 $\sigma_{\perp} = 111$ MPa

For the $(1\bar{1}1)_{Al}$ ($\alpha = 64^\circ$ and $\sigma = 155$ MPa):
 $\sigma_{\perp} = 139$ MPa

(3)

The resulting load difference between $(\bar{1}11)_{Al}$ and $(1\bar{1}1)_{Al}$ is 28 MPa

3.3.4. Strain Measurements Using GPA

To understand the thickening mechanism for T_1 precipitates, different stackings and thicknesses of the precipitates were analyzed with respect to the corresponding strain states. This was done by employing GPA analysis, which provides information on the local displacement in and around the

precipitates compared to the (stress free) reference Al matrix. In the following, the strain states for different stacking sequences are presented and used as an indication whether the lattice deformation in and around precipitates correlates to the stacking thickness or the stacking type. Figure 11 shows the comparison of ε_{yy} line profiles of defect free T_1 -Types (Figure 11a) and T_1 -Defect Types (Figure 11b) of stress-free aged samples. The matrix/precipitate interfaces are indicated by dashed vertical lines. It is clear in Figure 11 that the variations occur inside and outside of the precipitates, i.e., lattice planes within the T_1 plate as well as in the matrix are distorted in y -direction. It is evident that a significant increase in both the amplitude and the frequency of the variation of the ε_{yy} -component occurs as a function of the stacking height (i.e., precipitate thickness).

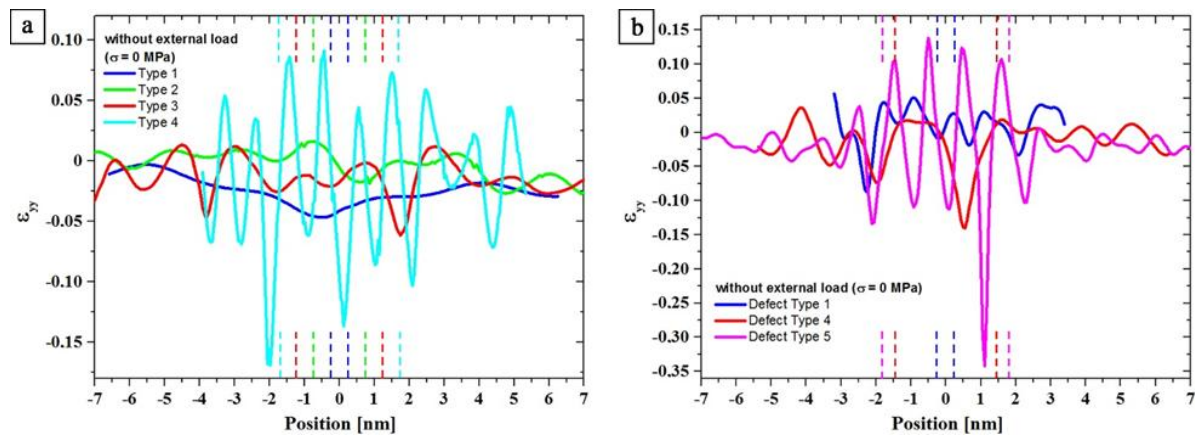


Figure 11. ε_{yy} line profiles for different thickness and stacking of T_1 precipitate types for load free aging: (a) defect free stacking (Types 1–4); and (b) T_1 stacking with defects (Defect Types 1, 4, and 5). Position 0 refers to the mid thickness ($c/2$). Vertical dashed lines indicate location of matrix/precipitate interface.

In Figure 11a, the smallest strain amplitude of about 5% is obtained for the stacking of T-1 (blue curve) and T-2 (green). The amplitude in strain variation increases slightly for T-3 (red) compared to the previous stacking types. For T-4 (turquoise), the strain variation is going up dramatically, up to five-fold the strain of T-1. Defect stacking DT-1 to DT-5 show similar characteristics (Figure 11b). The strain amplitude for DT-1 (blue) is about 6%, slightly more than the strain amplitude for the stacking T-1 and T-2. This means that thickening of DT-1 to DT-2 leads to a small reduction in strain energy. In fact, the T-2 stacking maintains the lowest strain among all different types of T_1 precipitate. Since during the stress-free isothermal heat treatment no T_1 precipitates with a stacking sequence of DT-2 and DT-3 were found, the next higher stacking is DT-4 (red). Its strain amplitude is about three times larger than the amplitude of DT-1. The highest strain amplitude for all T_1 stacking types is caused by DT-5 (magenta) which maintains a completely different defected stacking, as shown in Figure 8b.

4. Discussion

The precipitate phases formed in ternary Al–Cu–Li alloys depend on the Cu/Li ratio. For Cu/Li > 4 (on wt. % basis), the precipitation sequence is: $\alpha(ss) \rightarrow$ G.P. zones $\rightarrow \theta'' \rightarrow \theta' \rightarrow \theta$, with $\alpha(ss)$ being the supersaturated solid solution [1]. For Cu/Li ratios between 2.5 and 4, the reaction changes to: $\alpha(ss) \rightarrow$ G.P. zones \rightarrow G.P. zones + $\delta' \rightarrow \theta'' + \theta' + \delta' \rightarrow \delta' + T_1 \rightarrow T_1$. There is also evidence that, in certain ranges of composition at a given aging temperature, T_1 forms either in $(T_1 + \delta')$ or in $(T_1 + \theta')$ phase region. The Cu/Li ratio in the alloy investigated in this study is 4. In a previous study, we showed that, in our high-purity alloy, only θ' and T_1 are present in the PA state and no δ' is formed [33]. In addition, it is reported that the Li-content has to exceed >1.4% to form δ' , which is not the case in our alloy [1]. The current study shows that longer heat treatments beyond the PA state (both without and with external load) do not affect the phase formation, i.e., no other phases beside θ'

and T_1 are found. The volume fraction of θ' in our high-purity alloy is found to be higher than that of T_1 , which is different from results obtained in technical alloys (e.g., Al-alloy 2195, which has similar Cu, Li and Mn content but higher impurity level). It has to be noted that the aging temperature used in the present study is about 30 °C higher than the commonly used temperature, which might affect the precipitation sequence (i.e., the aging temperature may exceed the δ' solvus line).

Dorin et al. showed that, with an appropriate choice of alloy composition and thermomechanical treatment, the microstructure becomes dominated by T_1 precipitates [19]. Alloying elements such as Mg, Ag and/or Zr are known to serve as nucleation sites for the formation of T_1 resulting in T_1 being the dominant phase and the other phases are often not discussed due to their small amount. In the present study, the alloy was free of impurity elements, which means that the precipitates can only nucleate on lattice defects such as dislocations. This can be one reason the θ' phase occurred as the dominant phase.

Dorin et al. investigated the growth behavior of the T_1 precipitates as a function of time in a duplex aging treatment (at 155 °C and 190 °C) using SAXS measurements [42]. After 100 h, the system reached its maximum volume fraction. This agrees well with the observations of the present study, where the T_1 volume fraction remains unchanged after 257 h or even earlier (see Figure 9c). The volume fraction of T_1 in the crept specimens seems to be a little higher than in the load-free aged sample after 257 h and 1002 h. However, the difference is small and within the experimental error.

Similar to previous work [15,42], we also observed only single-layer T_1 precipitates after the PA treatment. The structures of the precipitates were, however, different (Table 3). In the present work, two types of single-layer T_1 precipitates, T-1 and DT-1 on the $\{111\}$ planes, were characterized in the PA state with thicknesses of 0.505 nm and 0.461 nm, respectively. While the structure of T-1 stacking confirms well the previous observations, the DT-1 stacking is not reported previously. For T-1 stacking, there are different structural models presented. In the Huang and Ardell [13] model, T-1 consists of an Al + Li layer surrounded by two Al + Cu layers and an Al + Li layer between the Al + Cu layer and the Al matrix. Howe et al. [12] supposed that T-1 is a pure Li layer surrounded by an Al + Cu layer. In both structural models, the Cu and Li atoms are disorderly distributed on the layers. The structural model of van Smaalen et al. [14] also assumes that a pure Li layer is surrounded by two Al + Cu layers. The difference to the model of Howe et al. is the displacement of Al atoms from the Al + Cu layer (with disordered Cu distribution) towards the central Li layer, i.e., a corrugated arrangement of the atoms. Furthermore, van Smaalen et al. assumed an Al + Li layer as a boundary layer to the Al matrix. Donnadiou et al. [15] analyzed HAADF images and SAXS results for all these models and found that the structure of the T-1 T_1 precipitate is well described by van Smaalen model [14]. The results however struggled with the composition and atomic arrangement at the precipitate/matrix interface.

A follow-up experimental and DFT study by Dwyer et al. [16] presents a different sequence in T_1 precipitates and resolved the discrepancy with respect to the composition of the interface layer. The Li-rich interfacial layer can only be imaged in $\langle 112 \rangle_{Al}$ orientation and is not observed in previous studies, as most of them focus on imaging in $\langle 110 \rangle_{Al}$ orientation. Furthermore, an extra layer of Al is observed close to the central Li layer in the T_1 precipitates that is necessary for obtaining thermodynamic stability of this phase. The HR-STEM images of the T_1 precipitates shown in the present work show no difference in intensity between the atomic columns of the Al matrix and that of the interfacial region of the T_1 precipitates. However, the T_1 precipitates were all imaged in $\langle 110 \rangle_{Al}$ orientation, in which the Li-sites in the interfacial layer are masked according to Dwyer et al. [16]. Recently, Kim et al. [17] suggested a modified structure of the van Smaalen model based on DFT studies that has a lower formation energy compared to all previous studies but only calculated at 0 K. However, a lack of understanding persists regarding the deformation processes at the interface layer of the T_1 precipitate, which transform it into a distorted plane in the Al $\{111\}$ matrix. The T_1 precipitate with T-1 stacking occupies a multiple of $\{111\}_{Al}$ atomic planes with $d_{\{111\}} = 0.223$ nm. Comparing this to the theoretical width obtained for the van Smaalen structure ($c = 0.9327$ nm) [17] and assuming a positive strain (considering five $\{111\}_{Al}$ atomic layer) one obtains $\varepsilon_{yy} = 0.19939$ (normal to

the precipitate plane), which is a relatively large value. On the other hand, assuming a negative strain (considering four $\{111\}_{\text{Al}}$ atomic layers), the strain becomes negligible ($\varepsilon_{yy} = -0.00075$). These are of course approximations since the other components of the structural deformation are not considered. Here the Li interfacial layers, which are displaced out-of-plane and towards the center of the precipitate can compensate the transformation strain.

The second type of single-layer T_1 precipitates found only in the PA state is the DT-1. It contains a bright intermediate layer and smaller thickness (0.461 nm versus 0.505 nm for T-1 stacking) that exhibits an Al-rich intermediate layer instead of Li or Al + Li.

Figure 7b shows a mixture of Type 1 and Defect Type 1 which suggests that the intermediate layer is progressively filled with Li atoms. This indicates that DT-1 can be a precursor of T-1, because it is only observed in the PA state (25% Defect Type 1 and 75% Type 1). Possibly, the parallel Al + Cu layers form first and Li atoms diffuse between the two Al + Cu layer in a later stage replacing Al atoms. During the filling with Li atoms, the Al atoms of the intermediate layer must now move towards the Al + Cu layers. Two diffusion paths are possible for this process: (1) perpendicular to the T_1 surface and thus through the Cu-rich layers; or (2) parallel to the Cu-rich layers. Diffusion Path (2) implies that T_1 plates with a large diameter grow slower in diameter than smaller ones: The lithium atoms have to reach the rim of the precipitate before they diffuse through them from the rim to the center of the precipitate.

The observation of DT-1 type and analysis of thicker T_1 precipitates suggests that the DT-1 stacking can be relatively stable, particularly next to the T-1 stacking. Although only 25% of T_1 precipitates in PA state were found to be of DT-1 type, this stacking seems to be a necessary step for thickening T_1 precipitate. Starting from a pre-existing DT-1, thickening can occur by the addition of a Cu layer (on the two sides of the precipitate) with an intermediate layer of Li atoms, i.e., a T-1 stacking. The resulting T_1 precipitates have a T-2 stacking as shown in Figure 8a. Alternatively, a T-1 precipitate can thicken to a T-2 by addition of a DT-1 and a T-1 stacking, sharing their Cu layers (see Figure 8a). Extending the aging from PA state for an extra 257 h, a thickening reaction occurred such that:



The thickness of T-2 stacking is found to be 1.471 nm = 2×0.505 nm + 0.461 nm, which confirms the above thickening sequence (see Figures 8a and 9b, and Table 4). In fact, T-1 and DT-1 stacking sequences are found to be elementary units of T_1 precipitation and all subsequent thickening occur by multiplying the T-1 and DT-1 stacking. In this picture, the interfacial Al + Li layer in the single T_1 precipitate, observed experimentally by Dwyer et al. [16], can rather belong to the Al matrix than the precipitate. This indeed explains the large distortion at the interface that was evidenced by Donnadiou et al. [15] as well as segregation of secondary alloying elements such as Ag at the interface [20].

The GPA results show that thickening is accompanied by a change of the strain field in and around the precipitates. The difference of the strain values $\varepsilon_{yy,max} - \varepsilon_{yy,min}$ was determined from the ε_{yy} line profiles, as shown in Figure 11. These strain difference values of all stacking types of T_1 are plotted as a function of precipitate thickness in Figure 12. One can see that strain difference value of the defect free stacking sequences after stress free aging (full blue squares) increases with precipitate thickness. For T-1 and T-2 stacking, the strain difference values are minimum. Indeed, the strain difference for T-2 stacking is slightly less than T-1 (4.3% and 4.4%, respectively) and DT-1 shows a somewhat higher strain difference value (6.0%). Hence, a reduction in the strain energy can be considered as one driving force for the thickening sequence [13].

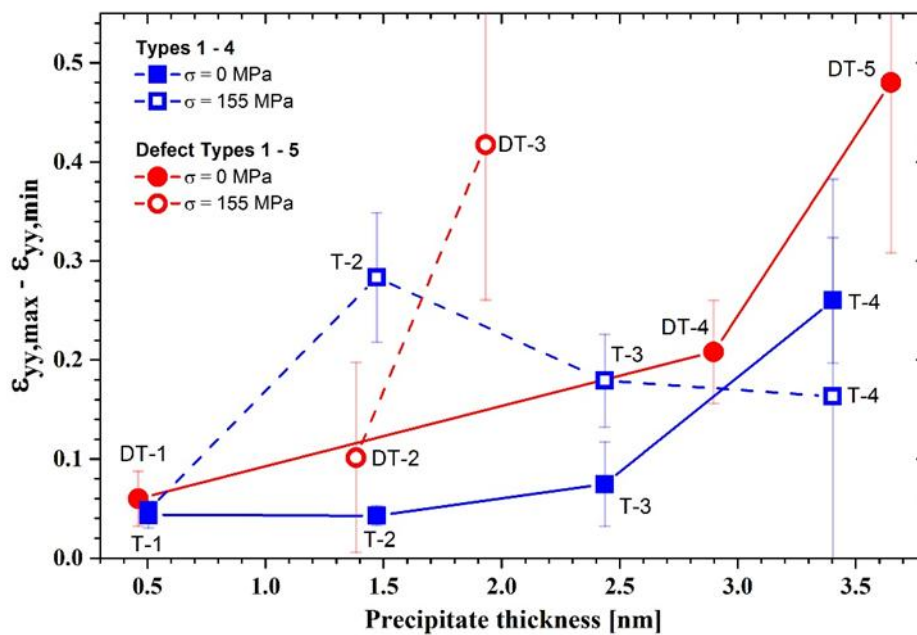


Figure 12. $\varepsilon_{yy,max} - \varepsilon_{yy,min}$ for different T_1 thickness and stacking after stress free aging and after creep testing calculated from the ε_{yy} line profiles in Figure 11. Blue, Types 1–4; red, Defect Types 1–5. Error bar for T-2 is smaller than symbol height.

A further thickening of T_1 precipitate is accompanied by a large increase in the strain difference. The increase of the stacking height from T-2 stacking to T-3, for instance, increases the strain difference to 7.5%. Further growth in thickness results in a strain difference of 26% for T-4. In fact, formation of T-3 and T-4 stacking was only observed after very long aging or in the presence of external load (Table 3).

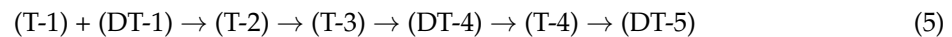
The application of an external load influences and disarranges the suggested sequence of thickening. The effect of external load enters evolution of precipitates in two ways [43]. If the system is heterogeneous, i.e., elastic constants of the precipitate and matrix phase differ, an external load σ generates an excess eigenstrain of $\sim \frac{\Delta\lambda}{\bar{\lambda}}\sigma$, where $\Delta\lambda$ is the difference in elastic modulus and $\bar{\lambda}$ is the average elastic modulus of the mixture. The second effect is due to volumetric energy introduced by the external load. While the first contribution leads to morphological modification of dispersed precipitates, the second contribution results in a change in the fractions of the precipitate and matrix phases.

According to Figure 12, stacking of T-4 appears to be energetically more favorable than T-2 and T-3 stacking in creep tested samples (open blue squares). Moreover, it appears that the DT-2 is energetically more favorable than the DT-3 in the crept specimens (open red circles). For the interpretation of the strain amplitude values of the crept specimens (red and blue open symbols in Figure 12), it has to be noted that the strains were measured after unloading and the direction and the magnitude of the external load which acts on the precipitates during aging under creep, was not taken into account. Thus, the selection of the reference region (REF) does not represent a strain-free region during the aging under load and the ε_{yy} measurements can only be taken as guide values in this case. To overcome this limitation, in-situ TEM studies have to be carried out, which were beyond the scope of the present study.

Furthermore, attention should be paid to the role of dislocations in the growth and thickening of T_1 precipitates that can facilitate nucleation of new layers on top of existing layers [10]. Dorin et al. [42] reported an abrupt acceleration in T_1 thickening, when increasing annealing temperature from 155 to 190 °C, while the rate of lengthening (diameter) of the precipitate was not changing much. This observation suggests a thermally activated mechanism of thickening which could involve the nucleation of a new layer on the surface of the precipitate. This nucleation barrier can be greatly

reduced when occurring at the intruding dislocations, as proposed by Cassada et al. [10,11]. Different studies have shown that the interaction among alloying elements, such as Mg, Cu and Zr, and dislocations can affect the nucleation of T_1 phase [21,44,45]. A similar influence on the thickening mechanism of the precipitate may be assumed, possibly involving a modified nucleation process. In this scenario, the contribution of solute atoms to the thickening can be either due to a reduction in interface energy or elastic energy (in the vicinity of the precipitate), as discussed by Bourgeois et al. [46] for θ' precipitation in a Sn-microalloyed Al-Cu system. Although secondary alloying elements are absent in the current alloy, it is likely that Li and/or Cu play a similar role, viz. reduces the interface energy, elastic energy or both, by segregating at the T_1 interface or around it, which leads to the observed thickening sequence in the current study.

Comparing the strain difference values of the defect-free T_1 structures (full blue squares) with those of the defected structures (full red symbols) after load-free aging, it is found that the defected structures (DTs) are associated with higher strain differences compared to the related defect free stacking (Figure 12). This interpretation is supported by the absence or small volume fraction of T_1 precipitates with defected structure after aging without load (Ref. 1 and 2, cf. Table 3). The thickening sequence of the T_1 precipitates in load-free isothermally treated samples is given by the increasing strain field/difference value as follows:



The analysis of strain differences suggests that the alternative sequence of the T-1 and DT-1 stacking, at least for T-2 and T-3 thickening can be driven by the reduction in the strain energy. In addition, the absence of DT-2 and DT-3 stacking can be explained by the formation of the energetically favored T-2 and T-3. Moreover, once the precipitates are of T-2 and T-3 stacking form, the stacking height for DT-2 and DT-3 has already been exceeded and the next stacking with defects is DT-4.

The current results show that the stacking sequence of the T_1 precipitates changes depending on the aging condition. The precipitates thicken with ageing time. In the current study, no ledges have been found on the T_1 precipitates while they were reported in early works of Cassada et al. [10,11]. The thickening of T_1 precipitates were previously observed after a duplex aging treatment (at 155 °C and 190 °C) [42]. The single-layer precipitate growth requires diffusion to the tip of the plates, while the thickening process requires diffusion to the broad faces of the (semi-)coherent interface [42].

Growth by ledges is well known for precipitate plates in different alloy systems [47]. The new phase must nucleate within a solid crystalline matrix and the nucleus has to minimize the interfacial free energy and the volume strain energy to overcome the activation barrier. Ledges are small mobile steps with coherent faces. Atomic transfer occurs across the disordered steps, resulting in a lateral movement of the ledges. Nucleation of ledges usually occurs heterogeneously, and the ledges may show a variety of configurations. The nucleation of ledges is difficult (even in technical alloys) and it is assumed that they form by a heterogeneous nucleation process [48]. Bourgeois et al. [46] showed that trace additions of certain elements may effectively support the ledge nucleation process. However, in our high-purity alloy, such elements are not available. The thickening often takes place by alternative stacking of T-1 and DT-1 single-layer plates. It seems that these alternative stacking is favored due to a reduction in elastic energy. The analysis of the strain differences (Figures 11 and 12) showed that a thickening to T-2 stacking results in a decrease of the strain amplitude around and within the precipitate while any further thickening leads to an increase. In the case of an external load, a higher number of stacks with defects was found in the crept specimens, which suggest that the accompanying lattice distortion energetically boosts the incorporation of defects into the stacking (Table 3).

The growth mechanisms appear to be different for the θ' precipitates. It has to be noted that formation and growth of θ' precipitates is characterized by a ledge mechanism [49], which allows the new phase to nucleate in the solid state phase transformation process. Dahmen and Westmacott [49] developed a model for θ' predicting that ledges of certain step height will form to minimize the transformation shape changes and volume changes.

External load affects formation and growth of the θ' precipitates. The experiments suggest that the length and arrangement of the precipitates is not much influenced by the external load (Figure 9a). This is due to the limited level of stress applied in this study. The volume fraction of the precipitates slightly increases under the external load (Figure 9c). The growth direction is roughly from the center to the rim of the precipitates (see Figure 13).

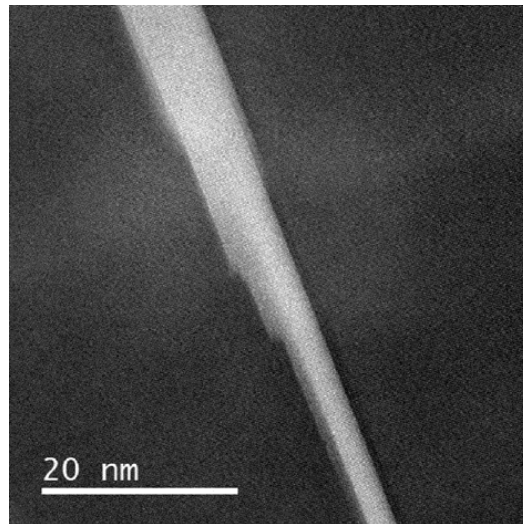


Figure 13. HAADF image of a θ' precipitate documenting that the growth mechanism is dominated by ledges formed at the interface.

5. Conclusions

In the present study, the evolution of T_1 and θ' precipitates was studied and quantified during aging at 180 °C for 257 h and 1002 h under load free and under creep conditions. The results were obtained using TEM, HR-STEM and GPA strain measurements and discussed in the light of previous studies. In particular, the structure and thickening sequence of T_1 precipitates were studied. The important findings are:

- Two elementary structures of single-layer T_1 precipitate were characterized, one with a Li-rich (T-1) and another with an Al-rich (DT-1) central layer. The T-1 structure is very similar to the structure proposed in the previous studies with a thickness of 0.505 nm. The DT-1 structure, however, is observed here for the first time and it has a thickness of 0.461 nm. Single-layer T_1 precipitates with mixture T-1 + DT-1 properties were observed as well that suggest DT-1 is a precursor for T-1 T_1 precipitate.
- It was found that the thickening of T_1 phase occurs by alternative stacking of the T-1 and DT-1 elementary structures. Based on the strain difference GPA measurements, a sandwich, T-2 = 2 (T-1) + (DT-1), T_1 precipitate is the most stable thickened precipitate. All precipitates after 257 h aging are found to be in this form.
- Upon longer aging, further thickening of T_1 precipitates was observed. Defected structures deviating from the alternative T-1 + DT-1 stacking sequence were observed as well, several of which were identified and studied in detail. In the absence of an external load, all thicker precipitates (including defected structures) carry a higher strain difference than T-2 stacking. In the presence of an external load, however, some of the defected structures form with lower strain difference that indicates they might have been preferred under loading condition. Furthermore, the frequency of precipitates with defected structures were found to be higher under loading condition.

While thickening occurs during aging, the length (diameter) of the T_1 and θ' precipitates were almost unchanged as compared to the PA state. Under external loading, the average length of T_1

precipitates increases but it remains almost unchanged for θ' precipitates. The volume fraction and the number density of T_1 seem not to be affected by an external stress. In contrast, creep loading for 257 h result in a 25% higher volume fraction and a 40% higher number density of θ' . The volume fractions for both precipitates saturate after 1002 h, which indicates that growth processes are completed.

Author Contributions: Conceptualization, I.H. and B.S.; Funding acquisition, R.D.K. and B.S.; Investigation, I.H. and W.H.; Supervision, B.S.; Writing—original draft, I.H.; and Writing—review and editing, R.D. K., W.H. and B.S..

Funding: This work was performed within the DFG Priority Program 1713 “Strong Coupling of Thermo-chemical and Thermo-Mechanical States in Applied Materials”. Financial support by the German Research Foundation is gratefully acknowledged (grant numbers DFG SK 47/10-1 and DFG DA 1655/1).

Acknowledgments: Thanks are due to Otto-Fuchs KG for producing the investigated material. We wish to thank S. Recknagel (BAM 1.6) for the wet chemical analysis; Daniela Valencia Ramirez and Benjamin Piesker for taking the hardness measurements and metallographic preparation of specimens; and J. Olbricht (BAM-5.2) for fruitful discussion and for carefully reading and correcting the manuscript. We would like to thank the working group of Rosenauer, University Bremen, for providing the ImageEval software.

Conflicts of Interest: The authors declare no conflict of interest.

References

1. Eswara Prasad, N.; Gokhale, A.A.; Wanhill, R.J.H. *Aluminum Lithium Alloys: Processing, Properties, and Applications*; Butterworth-Heinemann: Oxford, UK, 2014.
2. Noble, B.; Thompson, G.E. T_1 (Al_2CuLi) Precipitation in Aluminium–Copper–Lithium Alloys. *Metal Sci. J.* **1972**, *6*, 167–174. [[CrossRef](#)]
3. Noble, B.; McLauchlin, I.R.; Thompson, G. Solute atom clustering processes in aluminium-copper-lithium alloys. *Acta Metall.* **1970**, *18*, 339–345. [[CrossRef](#)]
4. Gable, B.M.; Csontos, A.A.; Starke, E.A., Jr. A quench sensitivity study on the novel Al–Li–Cu–X alloy AF/C 458. *J. Light Metals* **2002**, *2*, 65–75. [[CrossRef](#)]
5. Gable, B.M.; Zhu, A.W.; Csontos, A.A.; Starke, E.A., Jr. The role of plastic deformation on the competitive microstructural evolution and mechanical properties of a novel Al–Li–Cu–X alloy. *J. Light Metals* **2001**, *1*, 1–14. [[CrossRef](#)]
6. Yoshimura, R.; Konno, T.J.; Abe, E.; Hiraga, K. Transmission electron microscopy study of the early stage of precipitates in aged Al–Li–Cu alloys. *Acta Mater.* **2003**, *51*, 2891–2903. [[CrossRef](#)]
7. Yoshimura, R.; Konno, T.J.; Abe, E.; Hiraga, K. Transmission electron microscopy study of the evolution of precipitates in aged Al–Li–Cu alloys: The θ' and T_1 phases. *Acta Mater.* **2003**, *51*, 4251–4266. [[CrossRef](#)]
8. Ringer, S.P.; Muddle, B.C.; Polmear, I.J. Effects of Cold Work on Precipitation in Al–Cu–Mg–(Ag) and Al–Cu–Li–(Mg–Ag) Alloys. *Metall. Mater. Trans. A* **1995**, *26*, 1659–1671. [[CrossRef](#)]
9. Decreus, B.; Deschamps, A.; De Geuser, F.; Donnadiou, P.; Sigli, C.; Weyland, M. The influence of Cu/Li ratio on precipitation in Al–Cu–Li–x alloys. *Acta Mater.* **2013**, *61*, 2207–2218. [[CrossRef](#)]
10. Cassada, W.A.; Shiflet, G.J.; Starke, E.A. Mechanism of Al_2CuLi (T_1) nucleation and growth. *Metall. Trans. A* **1991**, *22*, 287–297. [[CrossRef](#)]
11. Cassada, W.A.; Shiflet, G.J.; Starke, E.A. The effect of plastic deformation on Al_2CuLi (T_1) precipitation. *Metall. Trans. A* **1991**, *22*, 299–306. [[CrossRef](#)]
12. Howe, J.M.; Lee, J.; Vasudevan, A.K. Structure and deformation behavior of T_1 precipitate plates in an Al–2Li–1 Cu alloy. *Metall. Trans. A* **1988**, *19*, 2911–2920. [[CrossRef](#)]
13. Huang, J.C.; Ardell, A.J. Crystal structure and stability of T_1 precipitates in aged Al–Li–Cu alloys. *Mater. Sci. Technol.* **1987**, *3*, 176–188. [[CrossRef](#)]
14. Van Smaalen, S.; Meetsma, A.; De Boer, J.L.; Bronsveld, P.M. Refinement of the crystal structure of hexagonal Al_2CuLi . *J. Solid State Chem.* **1990**, *85*, 293–298. [[CrossRef](#)]
15. Donnadiou, P.; Shao, Y.; De Geuser, F.; Botton, G.A.; Lazar, S.; Cheynet, M.; de Boissieu, M.; Deschamps, A. Atomic structure of T_1 precipitates in Al–Li–Cu alloys revisited with HAADF-STEM imaging and small-angle X-ray scattering. *Acta Mater.* **2011**, *59*, 462–472. [[CrossRef](#)]
16. Dwyer, C.; Weyland, M.; Chang, L.Y.; Muddle, B.C. Combined electron beam imaging and ab initio modeling of T_1 precipitates in Al–Li–Cu alloys. *Appl. Phys. Lett.* **2011**, *98*, 201909. [[CrossRef](#)]

17. Kim, K.; Zhou, B.-C.; Wolverton, C. First-principles study of crystal structure and stability of T₁ precipitates in Al-Li-Cu alloys. *Acta Mater.* **2018**, *145*, 337–346. [[CrossRef](#)]
18. Decreus, B.; Bley, F.; Deschamps, A.; Donnadiou, P. Phase Transformations: Quantitative Characterization of the Precipitation Kinetics in an AA2198 Al-Li-Cu Alloy. In Proceedings of the ICAA-11, Aachen, Germany, 22–26 September 2008; pp. 1040–1046.
19. Dorin, T.; Deschamps, A.; Geuser, F.D.; Sigli, C. Quantification and modelling of the microstructure/strength relationship by tailoring the morphological parameters of the T₁ phase in an Al-Cu-Li alloy. *Acta Mater.* **2014**, *75*, 134–146. [[CrossRef](#)]
20. Kang, S.J.; Kim, T.-H.; Yang, C.-W.; Lee, J.I.; Park, E.S.; Noh, T.W.; Kim, M. Atomic structure and growth mechanism of T₁ precipitate in Al-Cu-Li-Mg-Ag alloy. *Scr. Mater.* **2015**, *109*, 68–71. [[CrossRef](#)]
21. Araullo-Peters, V.; Gault, B.; Geuser, F.D.; Deschamps, A.; Cairney, J.M. Microstructural evolution during ageing of Al-Cu-Li-x alloys. *Acta Mater.* **2014**, *66*, 199–208. [[CrossRef](#)]
22. Blum, W. Creep of aluminium and aluminium alloys. In Proceedings of the Symposium on Hot Deformation of Al-Alloys, TMS Fall Meeting, Detroit, MI, USA, 8–12 October 1990; pp. 1–29.
23. Morris, M.A.; Martin, J.L. Evolution of internal stresses and substructure during creep at intermediate temperatures. *Acta Metall.* **1984**, *32*, 549–561. [[CrossRef](#)]
24. Morris, M.A.; Martin, J.L. Microstructural dependence of effective stresses and activation volumes during creep. *Acta Metall.* **1984**, *32*, 1609–1623. [[CrossRef](#)]
25. Blum, W.; Rosen, A.; Cegielska, A.; Martin, J.L. Two mechanisms of dislocation motion during creep. *Acta Metall.* **1989**, *37*, 2439–2453. [[CrossRef](#)]
26. Mills, M.J.; Gibeling, J.C.; Nix, W.D. A dislocation loop model for creep of solid solutions based on the steady state and transient creep properties of Al-5,5 at. % Mg. *Acta Metall.* **1985**, *33*, 1503–1514. [[CrossRef](#)]
27. Mills, M.J.; Gibeling, J.C.; Nix, W.D. Measurement of anelastic creep strains in Al-5,5 at. % Mg using a new technique: Implications for the mechanism of class I creep. *Acta Metall.* **1986**, *34*, 915–925. [[CrossRef](#)]
28. Skrotzki, B. *Mechanical Loading of Light Alloys at Elevated Temperature*; VDI-Verlag GmbH: Düsseldorf, Germany, 2001; Volume 629.
29. Skrotzki, B.; Murken, J. On the Effect of Stress on Nucleation, Growth, and Coarsening of Precipitates in Age-Hardenable Aluminum Alloys. In *Lightweight Alloys for Aerospace Application*; Jata, K., Lee, E.W., Frazier, W., Kim, N.J., Eds.; Wiley: Hoboken, NJ, USA, 2013.
30. Skrotzki, B.; Shiflet, G.; Starke, E. On the effect of stress on nucleation and growth of precipitates in an Al-Cu-Mg-Ag alloy. *Metall. Mater. Trans. A* **1996**, *27*, 3431–3444. [[CrossRef](#)]
31. Tsivoulas, D. Heterogeneous Nucleation of the T₁ Phase on Dispersoids in Al-Cu-Li Alloys. *Metall. Mater. Trans. A* **2015**, *46*, 2342–2346. [[CrossRef](#)]
32. Dorin, T.; De Geuser, F.; Lefebvre, W.; Sigli, C.; Deschamps, A. Strengthening mechanisms of T₁ precipitates and their influence on the plasticity of an Al-Cu-Li alloy. *Mater. Sci. Eng. A* **2014**, *605*, 119–126. [[CrossRef](#)]
33. Häusler, I.; Schwarze, C.; Umer Bilal, M.; Valencia Ramirez, D.; Hetaba, W.; Darvishi Kamachali, R.; Skrotzki, B. Precipitation of T₁ and θ' Phase in Al-4Cu-1Li-0.25Mn During Age Hardening: Microstructural Investigation and Phase-Field Simulation. *Materials* **2017**, *10*, 117. [[CrossRef](#)]
34. *DIN EN ISO 6506-1: Metallic Materials—Brinell Hardness Test—Part 1: Test Method*; Beuth Verlag GmbH: Berlin, Germany, 2015.
35. Williams, D.B.; Carter, C.B. *Transmission Electron Microscopy*; Springer: Boston, MA, USA, 2009.
36. Castro Riglos, M.V.; Tolley, A. A method for thin foil thickness determination by transmission electron microscopy. *Appl. Surf. Sci.* **2007**, *254*, 420–424. [[CrossRef](#)]
37. Häusler, I. Determination of volume fraction of discrete oriented circular disc-shaped precipitates in the transmission mode. *Pract. Metallogr.* **2017**, *54*, 816–837. [[CrossRef](#)]
38. Hýtch, M.J.; Snoeck, E.; Kilaas, R. Quantitative measurement of displacement and strain fields from HREM micrographs. *Ultramicroscopy* **1998**, *74*, 131–146. [[CrossRef](#)]
39. Müller-Caspary, K.; Mehrtens, T.; Schowalter, M.; Grieb, T.; Rosenauer, A.; Krause, F.F.; Mahr, C.; Potapov, P. ImageEval. A software for the processing, evaluation and acquisition of (S)TEM images. In *European Microscopy Congress 2016: Proceedings—Instrumentation and Methods*; Wiley-VCH Verlag GmbH & Co.: Weinheim, Germany, 2016; pp. 481–482.
40. Gao, Z.; Liu, J.Z.; Chen, J.H.; Duan, S.Y.; Liu, Z.R.; Ming, W.Q.; Wu, C.L. Formation mechanism of precipitate T₁ in AlCuLi alloys. *J. Alloys Compd.* **2015**, *624*, 22–26. [[CrossRef](#)]

41. Liu, C.; Malladi, S.K.; Xu, Q.; Chen, J.; Tichelaar, F.D.; Zhuge, X.; Zandbergen, H.W. In-situ STEM imaging of growth and phase change of individual CuAl_x precipitates in Al alloy. *Sci. Rep.* **2017**, *7*, 2184. [[CrossRef](#)] [[PubMed](#)]
42. Dorin, T.; Deschamps, A.; De Geuser, F.; Lefebvre, W.; Sigli, C. Quantitative description of the T_1 formation kinetics in an Al-Cu-Li alloy using differential scanning calorimetry, small-angle X-ray scattering and transmission electron microscopy. *Philos. Mag.* **2014**, *94*, 1012–1030. [[CrossRef](#)]
43. Li, D.Y.; Chen, L.Q. Shape evolution and splitting of coherent particles under applied stresses. *Acta Mater.* **1998**, *47*, 247–257. [[CrossRef](#)]
44. Gumbmann, E.; Lefebvre, W.; De Geuser, F.; Sigli, C.; Deschamps, A. The effect of minor solute additions on the precipitation path of an AlCuLi alloy. *Acta Mater.* **2016**, *115*, 104–114. [[CrossRef](#)]
45. Itoh, G.; Cui, Q.; Kanno, M. Effects of a small addition of magnesium and silver on the precipitation of T_1 phase in an Al-4%Cu-1.1%Li-0.2%Zr alloy. *Mater. Sci. Eng. A* **1996**, *211*, 128–137. [[CrossRef](#)]
46. Bourgeois, L.; Dwyer, C.; Weyland, M.; Nie, J.-F.; Muddle, B.C. The magic thicknesses of θ' precipitates in Sn-microalloyed Al-Cu. *Acta Mater.* **2012**, *60*, 633–644. [[CrossRef](#)]
47. Shiflet, G.J.; Mangan, M.A.; Meng, W.G. Growth by Ledges. *Interface Sci.* **1998**, *6*, 133–154. [[CrossRef](#)]
48. Porter, D.A.; Easterling, K.E. *Phase Transformations in Metals and Alloys*, 2nd ed.; Chapman & Hall: London, UK, 1993.
49. Dahmen, U.; Westmacott, K.H. Ledge structure and the mechanism of θ' precipitate growth in Al-Cu. *Phys. Status Solidi A* **1983**, *80*, 249–262. [[CrossRef](#)]



© 2018 by the authors. Licensee MDPI, Basel, Switzerland. This article is an open access article distributed under the terms and conditions of the Creative Commons Attribution (CC BY) license (<http://creativecommons.org/licenses/by/4.0/>).